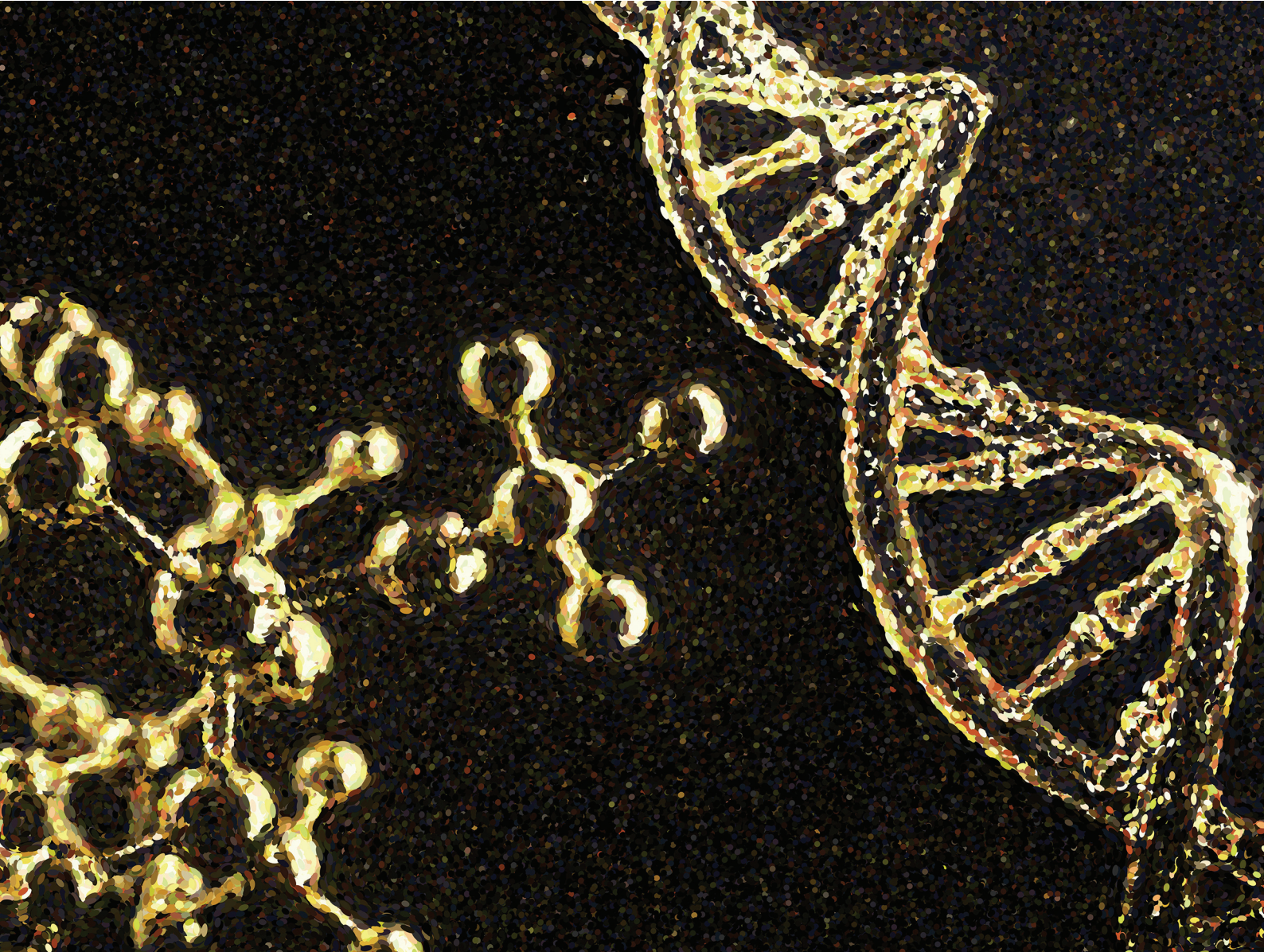


# Polymer Chemistry

[rsc.li/polymers](http://rsc.li/polymers)



ISSN 1759-9962



Cite this: *Polym. Chem.*, 2024, **15**, 2627

Received 21st February 2024,  
Accepted 16th May 2024

DOI: 10.1039/d4py00196f

rsc.li/polymers

We present a class of programmable polymer nanoparticles capable of intravenous pDNA delivery with ~350 000-fold enhancement of specificity to the lung by qPCR in mice. Molecular level insight of these polyelectrolytes is connected to bioperformance, exemplifying how robust, data-driven workflows can expedite synthesis/screening campaigns for gene therapy.

The scarcity of safe, effective delivery technologies is the single largest barrier to the development of a new wave of genetic therapies. Significant shortcomings exist in current modalities including immunogenicity and payload size limitations for viral vectors,<sup>1</sup> and manufacturing and intellectual property constraints for lipid nanoparticles.<sup>2</sup> Furthermore, the vast majority of nonviral delivery systems are cleared by the liver *via* hepatic clearance after systemic administration,<sup>3</sup> presenting significant challenges for non-hepatic gene delivery. This feature can be somewhat mitigated by controlling the nanocarriers' physical characteristics (such as size/shape<sup>4</sup> or PEGylation<sup>5</sup>), adopting active targeting strategies,<sup>6</sup> or by exploiting circulating plasma protein interactions *in vivo*.<sup>7</sup> However, it remains unclear how a genetic cargo packed within heterogeneous nanocarriers overcomes extracellular barriers to reach the intended site of action. This biodistribution challenge has been well recognized in nanomedicine for decades.<sup>8</sup> To expand tropism outcomes to clinically relevant gene therapy targets such as the spleen,<sup>9</sup> lungs,<sup>10</sup> heart,<sup>11</sup> eye,<sup>12</sup> or nervous system,<sup>13</sup> greater investigation of the biological consequences from the integrated chemical and biophysical features of nanoparticles is needed.

Polymer nanoparticles (PNPs, or polyplexes formed from tailored cationic polymers and therapeutic nucleic acids) offer distinct advantages as multifunctional delivery systems.<sup>14,15</sup> Advanced polymer chemistry techniques now offer access to nearly any conceivable chain structure and architecture from a

diverse array of building blocks.<sup>16,17</sup> Despite these synthetic advances, there remain two major limitations to wider adoption of polymers as gene therapy excipients. First, the chemical design space of organic small molecules relevant to drug delivery<sup>18</sup> is estimated to be on the order of  $10^{60}$ —a vast number that, even if reduced to more surmountable subsets *via* exhaustive data mining, cannot be practically interrogated with the current state of polymer informatics.<sup>19</sup> Second, *in vitro* cellular assays, while amenable to high-throughput screening for highly valuable transfection data across cell types,<sup>20,21</sup> often provide poor predictions on the crossing of complex physiological barriers *in vivo*.<sup>22,23</sup> Thus, unclear *in vitro*–*in vivo* correlation results represent a difficult obstacle in PNP optimization in translating genetic drugs from cellular level assays to living systems.

In this communication, we report the discovery of a three-component polyelectrolyte system that was identified while developing PNP candidates for localization to the lung. Nanite's proprietary platform SAYER<sup>TM</sup> couples experimental data generation with artificial intelligence (AI) to identify high-performing PNPs for efficient delivery of diverse genetic cargo to tissues outside of the liver<sup>24</sup> (Fig. 1). The details of how PNP

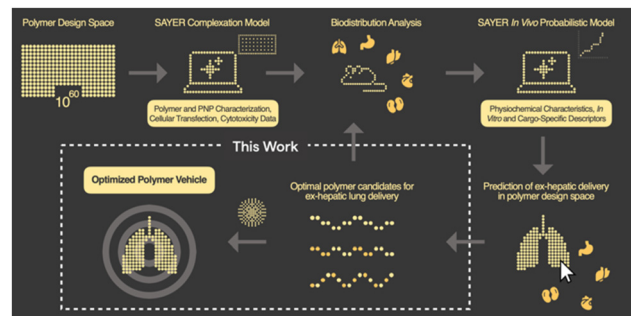


Fig. 1 Overview of designing tissue-specific gene delivery polymer nanoparticles using data-driven workflows and prediction from *in vivo* screening. This work shows how lead polymer candidates are characterized and optimized for lung delivery.

Nanite, Inc., Boston, Massachusetts 02109, USA. E-mail: jeff@nanitebio.com

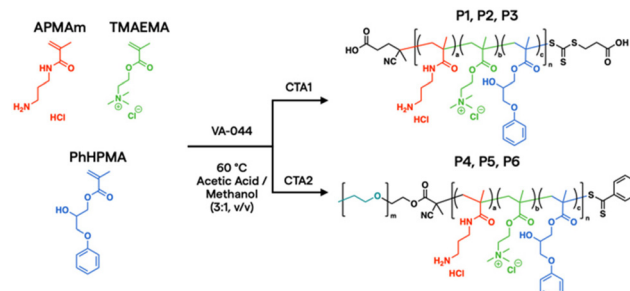
† Electronic supplementary information (ESI) available. See DOI: <https://doi.org/10.1039/d4py00196f>

complexation, *in vitro*, and *in vivo* probabilistic models predict ex-hepatic delivery from the vast polymer design space are described elsewhere.<sup>25,26</sup> Large chemical, materials, and biological datasets are stored and used for PNP down-selection and screening in our general workflow. We focus here on developing a *mechanistic* understanding of this polyelectrolyte candidate, and establish structure–property relationships that support nonintuitive design strategies for potent therapeutic PNPs with lung specificity. This framework further reveals new AI opportunities for universal tissue-specific gene delivery.

The conventional paradigm to design polymeric systems for gene delivery is to combine cationic interactions offered by alkyl substituted amine,<sup>27,28</sup> imidazolium,<sup>29,30</sup> guanidinium,<sup>31,32</sup> or even non-nitrogenous monomers (*e.g.*, sulfonium,<sup>33,33</sup> phosphonium<sup>34,35</sup>) with hydrophilic, hydrophobic, or stimuli-responsive comonomers.<sup>36–39</sup> The general rationale is to balance trends in charge type and density trends against complementary polymer/cargo associations in solution. In the current work, we took a broader approach by generating not only two-component polyelectrolytes to test traditional PNP hypotheses, but also multimonomeric statistical analogs, which are known to offer rich (and sometimes, unintuitive) dynamics in solution.<sup>40,41</sup> By scanning a more diverse landscape of multimonomeric polyelectrolytes, we aimed to determine whether unique PNP assemblies can be trafficked to the lung with minimal liver accumulation *via* systemic administration. Lung-specific delivery is often attributed to the entrapment of large nanoparticles in pulmonary capillaries,<sup>4,42</sup> a passive targeting approach that is difficult to recapitulate *in vitro*. In the present work we aimed to rigorously generate polymers that do not rely solely on passive targeting to deliver pDNA to the lung.

In the current work, aqueous reversible addition–fragmentation chain transfer (RAFT) polymerization<sup>43,44</sup> was employed to prepare a prototypical library *via* automated liquid handling.<sup>45,46</sup> After screening over 1300 polymers synthesized in house and digitally labelled for training AI models from PNP characterization, *in vitro* assays, and *in vivo* biodistribution data,<sup>24</sup> unique monomer candidates emerged for plasmid DNA (pDNA) delivery, based on *N*-(3-aminopropyl)methacrylamide hydrochloride (APMAM), 2-(trimethylammonio)ethyl methacrylate chloride (TMAEMA), and 3-phenoxy-2-hydroxypropyl methacrylate (PhHPMA). APMAM offers a pH-responsive primary amine that is expected to bind strongly to nucleic acids. TMAEMA exhibits a permanently charged ammonium group that can assist with cellular uptake. PhHPMA provides complementary non-covalent interactions in hydrophobicity and hydrogen bonding through an aromatic ring and hydroxyl group. However, it was unclear how to combine them at the nanoscopic level to assemble with pDNA into PNP candidates for lung delivery.

To further characterize the properties and behavior of the APMAM/TMAEMA/PhHPMA polymer, a series of six representative samples were prepared (Scheme 1). For close consistency with the degree of polymerization (DP) and compositions of a polymer library investigated by Kumar *et al.*,<sup>25</sup> we targeted



Scheme 1 RAFT synthesis of multimonomeric polyelectrolytes.

DP = 80 using thermal initiator VA-044 and RAFT chain transfer agents 4-(((2-carboxyethyl)thio)carbonothioyl)thio)-4-cyano-pentanoic acid (CTA1) and poly(ethylene glycol) (PEG) 4-cyano-4-(phenylcarbonothioylthio) pentanoate (CTA2) at a 10:1 molar ratio for 18 h. PEG coatings in micellar PNPs are known to inhibit aggregation in the blood and prolong circulation.<sup>47</sup> The inclusion of PEG allows for modulation of colloidal nanoparticle sizes from known physical scaling laws of polyelectrolyte complex micelles,<sup>48</sup> where the charged block length predominately drives its core size. PEGylated PNPs can condense pDNA payloads into 10–100 nm discrete domains depending on chemistry and solution conditions.<sup>49</sup> As shown in Table 1, we varied APMAM/PhHPMA ratios at fixed TMAEMA for non-PEGylated polymers (P1, P2, and P3) and PEGylated block polymers (P4, P5, and P6) so that the total charge (*i.e.*, APMAM + TMAEMA) was 75, 50, and 25 mol% relative to neutral PhHPMA. By aqueous size-exclusion chromatography PEGylated samples show a reasonable molar mass ( $M_n \sim 10\text{--}20 \text{ kg mol}^{-1}$  relative to PEG standards) with reasonable dispersity ( $D \leq 1.4$ ). We were unable to quantify the molar mass of P1–P3 due to known solubility challenges<sup>43,44</sup> of multicomponent water-soluble polymers and column interactions.

Because reactions were carried out to near complete conversion, we chose to investigate the statistical distribution of monomers by measuring pairwise reactivity ratio ( $r$ ) values and evaluating composition drift effects.<sup>50</sup> This approach has previously demonstrated utility in characterizing multimonomeric RAFT polymers that can impart various non-covalent interactions.<sup>51,52</sup> Three standard radical polymerization runs

Table 1 Polymer characterization summary

| ID | PEG (DP) | Polyelectrolyte (DP) <sup>a</sup> |        |        |                               |     |
|----|----------|-----------------------------------|--------|--------|-------------------------------|-----|
|    |          | APMAM                             | TMAEMA | PhHPMA | $M_n$ (kg mol <sup>-1</sup> ) | $D$ |
| P1 | 0        | 52                                | 8      | 20     | 14.1 <sup>b</sup>             | —   |
| P2 | 0        | 32                                | 8      | 40     | 15.1 <sup>b</sup>             | —   |
| P3 | 0        | 12                                | 8      | 60     | 16.2 <sup>b</sup>             | —   |
| P4 | 45       | 52                                | 8      | 20     | 9.86                          | 1.3 |
| P5 | 45       | 32                                | 8      | 40     | 10.4                          | 1.4 |
| P6 | 45       | 12                                | 8      | 60     | 19.9                          | 1.3 |

<sup>a</sup> Based on targeted feed ratio. <sup>b</sup> Targeted molecular weight; samples not fully soluble in tested aqueous mobile phase.

were conducted for each monomer combination, keeping total monomer conversion below  $\sim 15\%$ . The monomers' conversion from the initial feed composition ( $f$ ) and polymer composition ( $F$ ) were assessed by  $^1\text{H}$  NMR spectroscopy (see ESI<sup>†</sup>). We fitted the data directly to the Copolymerization equation  $F_1 = (r_{12}f_1^2 + f_1f_2)/(r_{12}f_1^2 + 2f_1f_2 + r_{21}f_2^2)$ . We further constructed Mayo-Lewis plots (Fig. S3<sup>†</sup>) and determined the  $r$  values under these specific reaction conditions to be  $r_{\text{APMAm-TMAEMA}} = 0.38 \pm 0.02$ ,  $r_{\text{APMAm-PhHPMA}} = 1.01 \pm 0.32$ ,  $r_{\text{TMAEMA-APMAm}} = 0.14 \pm 0.02$ ,  $r_{\text{TMAEMA-PhHPMA}} = 0.52 \pm 0.16$ ,  $r_{\text{PhHPMA-APMAm}} = 1.59 \pm 0.51$ , and  $r_{\text{PhHPMA-TMAEMA}} = 0.13 \pm 0.08$ .

Determination of  $r$  values allows us to describe the polymers' microstructure and reveal the consequences of compositional drift from carrying out RAFT polymerizations to high conversion. Smith *et al.* developed a practical visualization tool using Monte Carlo methods from measured  $r$  values.<sup>53</sup> This compositional drift program uses the relative reactivities from  $r$  values, adding one repeat unit from a large pool of monomers (set to 200 000) to growing chains per activation/deactivation cycle. Fig. 2A–C shows the results for P1, P2, and P3. For the charged monomers, we observe that TMAEMA (green) are quickly incorporated into polymer chains as single units, whereas APMAm (red) are distributed throughout the chain. For instance, the instantaneous polymer composition of P2 at 10% and 50% conversion are 0.37/0.26/0.37 and 0.36/0.06/

0.58 mole fractions of APMAm/TMAEMA/PhHPMA, respectively. It is also clear that depending on the targeted composition seen in P1 and P3, the APMAm and PhHPMA blockiness run lengths can be modulated. Unreacted TMAEMA monomers are quickly consumed as the target composition decreases, whereas APMAm is added throughout monomer conversion (Fig. 2D). This observation implies that ammonium moieties are physically localized in the resultant chains' microstructure because of the relative reactivities of monomers under these reaction conditions. For PEGylated polymers, TMAEMA units are incorporated into the chain closer to the PEG block.

Based on the multiple chain instantiations of the Monte Carlo simulation,<sup>53</sup> we computed the probability of a monomer  $X$  polymerized in a chain position  $i$  as  $p(X_i)$ . Thus, for monomer  $j$  in polymer  $P$ , the Shannon entropy of the monomer is given by:  $H(X) = -\sum p(X_i) \log(p(X_i))$ . The Shannon entropy will be higher for coconstitutional monomers that are randomly distributed across the polymer. Fig. 2E presents the calculated entropies for each monomer in each polymer. TMAEMA shows the lowest entropy across P1, P2 and P3, confirming its physical localization and early depletion in the resultant chain microstructures.

Such insights are challenging to obtain experimentally but may offer a unique feature of multimonomeric polyelectrolytes' ability to control complexation dynamics. From random phase

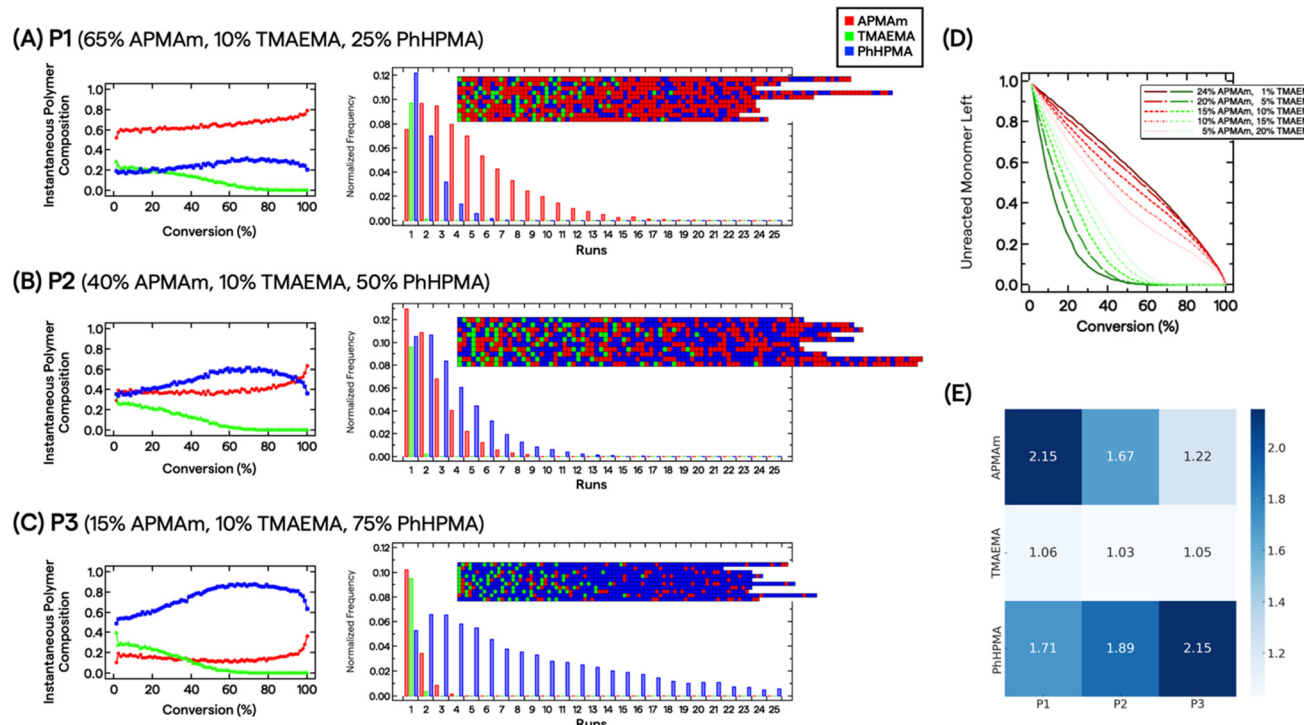


**Fig. 2** Predicted distribution of APMAm (red), TMAEMA (green), and PhHPMA (blue) using the compositional drift program for (A) P1, (B) P2, and (C) P3 from determined reactivity ratios. In (A)–(C) on the left, plots show the instantaneous polymer composition as a function of monomer conversion; on the right, Monte Carlo simulation results show the normalized frequency of monomers as a function of run lengths; in the inset ten representative simulated chains are shown from a pool of 200 000 monomers. (D) For simulated P3 chains, the effect of varying the APMAm/TMAEMA charge composition for the unreacted monomers remains tunable as a function of monomer conversion. (E) Heatmap array plot shows the calculated Shannon entropy of constituent monomers (left) for corresponding polymers P1–P3 (bottom); darker blue indicates higher entropy.

approximation theory and molecular dynamics simulations, random polyelectrolyte sequences are expected to have a dramatic effect on the cooperativity of Coulomb interactions between oppositely charged macromolecules.<sup>54,55</sup> While we do not dwell on polyelectrolyte phase behavior in this current work, compositional drift can potentially offer more fundamental understanding of the statistical distribution of charges in multimonomeric polymers, for not only gene therapy but also wastewater treatment/purification strategies,<sup>56</sup> viral vaccine formulation,<sup>57</sup> and enhancing viscoelastic response in coacervation.<sup>58</sup> Here, we hypothesize that blocky attributes of P1 and P3 (as well as their PEGylated analogs P4 and P6) can influence not only pDNA stabilization, but also blood plasma protein interactions, distinguishing them from random binary polyelectrolytes.

We next formed PNPs with enhanced-green fluorescent protein (EGFP)-encoding pDNA and evaluated complexation. Ionic strength and buffer additives are known to affect polyelectrolyte assembly formation and stability of phase separation over time.<sup>49,59</sup> To this end, all PNPs were prepared at N/P (the ratio of the nitrogen on polymer to the phosphate on nucleotide) of 5 as a starting point from previous work<sup>25</sup> for structural analysis under various solution conditions. We mixed P1–P6 with pDNA to form nanoparticles PNP1–PNP6. The size distributions of PNP1–PNP6 were characterized using dynamic light scattering (DLS) in an automated plate reader as a function of added salt (50, 100, and 250 mM NaCl) and sugar (0, 5, 10% glucose) after 30 min equilibration. Adding salt and sugar provides annealing<sup>60</sup> and isotonicity<sup>61</sup> for bio-applications, respectively. The apparent mean hydrodynamic radius ( $R_h$ ) and polydispersity (PDI) were determined from a cumulant fitting to DLS autocorrelation functions that exhibited a single decay. Fig. 3 shows a representative size comparison of PNPs as a function of NaCl at 25 °C. Non-PEGylated PNP1–3 showed evidence of aggregation from 50 to 100 mM NaCl, followed by size reduction at 250 mM NaCl suggesting complex disassembly. We therefore excluded these from consideration for preliminary *in vivo* testing. By comparison, the mean  $R_h$  of PEGylated PNP4–6 grew by ~15–20% as NaCl

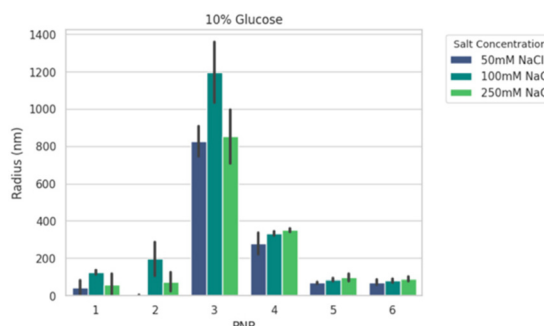


Fig. 3 Representative summary of the apparent radius of PNP1–PNP6 with 50, 100, and 250 mM added NaCl at 10% added glucose at 25 °C. All values show the mean + standard deviation of 15 acquisitions from dynamic light scattering.

increased from 50 to 250 mM. Of these samples, PNP5 and PNP6 were the smallest (70–90 nm) and most salt resistant (PDI 0.3–0.4). Overall size and stability did not vary strongly as a function of added sugar, temperature, or CaCl<sub>2</sub>, a divalent salt that disrupts short-range cation–π interactions.<sup>59,62</sup> To make a decision on prioritizing PNP testing *in vivo*, we performed high-content analysis of conventional HEK293T cells across all PNPs as a function of N/P = 1.25 to 40 (Fig. S18†). The mean effective transfection capability by EGFP expression *in vitro* was demonstrated for PNP5 (14% at N/P = 2.5) and PNP6 (19% at N/P = 20), with PNP6 showing less cytotoxicity at higher N/P (Fig. S19†). Because of the multiplicity of PNP properties that may impact *in vitro* translation to *in vivo* delivery to the lung, we limit discussions of transfection here and direct interested readers to the ESI† for full details.

With an understanding of polymer features, PNP properties, and trained AI models, we down selected PNP6 to be tested as a proof-of-concept for *in vivo* biodistribution of pDNA (5 µg dose) in 10 mice *via* intravenous administration. After 6 h, major organs (liver, lung, spleen, heart, and kidney) were harvested and analyzed. Fig. 4A shows the biodistribution from processed organs using real-time quantitative polymerase chain reaction (qPCR). We analyzed gene expression using the

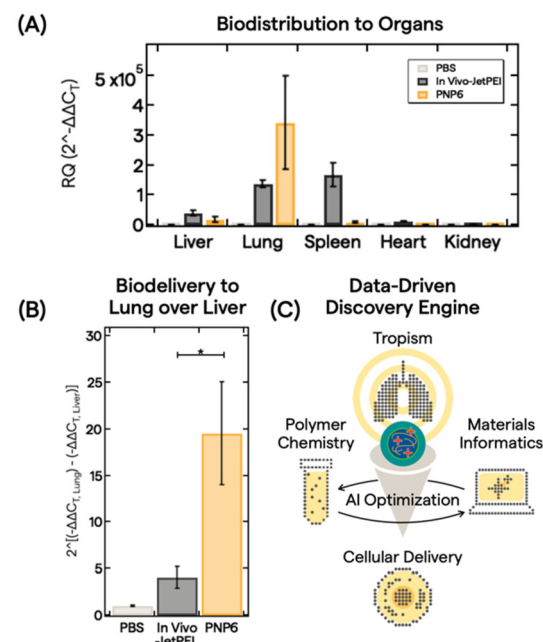


Fig. 4 Delivery of PNP6 *in vivo*. (A) Biodistribution data of PBS (light gray), In Vivo-JetPEI (dark gray), and PNP6 (dark yellow) in major organs (liver, lung, spleen, heart, and kidney) in mice. pDNA tissue accumulation was quantified by qPCR DNA amplification using the  $2^{(\Delta\Delta C_T)}$  method for analyzing the fold change in pDNA delivery. All values show the mean + standard error of the mean for  $N = 3$  (PBS, JetPEI) or  $N = 4$  (PNP6). (B) Evaluation of ex-hepatic delivery with the  $2^{(\Delta\Delta C_T)}$  method by taking the mean difference between the  $-\Delta\Delta C_T$  lung and the  $-\Delta\Delta C_T$  liver values for PBS, JetPEI, and PNP6. \* denotes statistical significance using Student's *t*-test at  $p = 0.05$ . (C) Use of PNP lung specificity in AI optimization with polymer chemistry and MI for downstream cellular delivery.

conventional relative quantification (RQ) or  $2^{(-\Delta\Delta C_t)}$  method.<sup>63</sup> Here,  $2^{(-\Delta\Delta C_t)}$  is defined as the fold change in pDNA delivered between the treatment group and a control group, in this case, PBS buffer only. See the ESI† for full qPCR analysis details. *In vivo*-JetPEI, a commercial gold standard polyethylenimine optimized for *in vivo* gene delivery, served as the positive control. While the *in vivo*-JetPEI PNP exhibited broad gene delivery in the liver, lung, and spleen, PNP6 delivered pDNA cargo near exclusively to the lung with a ~350 000-fold enhancement of specificity. Fig. 4B presents a linear comparison of this enhancement in the exponential gene delivery process to illustrate the remarkable ex-hepatic delivery of PNP6 to the lung. PNP6 outperforms *in vivo*-JetPEI by a factor of 4 with statistical significance ( $p < 0.05$ ). High lung-selectivity is also shown relative to all other major organs (Fig. S17).

We trace this exceptional lung specificity to the inherent molecular design of PNP6. From literature ref. 64–66, it appears that polymer- and lipid-based nanocarriers containing ammonium motifs show lung targeting upon intravenous administration. Cao *et al.* showed exquisite mRNA delivery to the lung using poly(β-amino esters) (PBAEs) as hydrophobic helper polymers with DOPAT (2-(dodecylthiocarbonothioylthio)propanoic acid), a lipid comprising a quaternary ammonium headgroup.<sup>64</sup> Analogously, Dilliard *et al.* demonstrated selective lung targeting of mRNA LNPs by formulating DOPAT into conventional 4-component LNP formulations.<sup>65</sup> By altering the surface chemistry of PBAEs or LNPs and analyzing animal plasma proteins, both groups showed how DOTAP promotes vitronectin corona formation, which binds to the  $\alpha\beta\beta$  integrin present in pulmonary endothelium (but not liver or other vascular cells). We believe that the multimonomeric polyelectrolytes, with carefully tailored APMAm, TMAEMA, and PhHPMA compositions such as in PNP6, can exploit similar design principles as nanocarriers without exhaustive formulation efforts. Further strategies, such as blending polymers for bioenhancement<sup>67,68</sup> or bioconjugation to adopt endosomolytic agents,<sup>68,69</sup> can then be carried out to selectively increase targeted delivery to cells of interest.

These findings demonstrate an attractive approach to deliver clinically relevant genetic cargo to the lung, thereby expanding potential non-viral treatments for genetic disorders such as cystic fibrosis.<sup>70</sup> Using a data-driven discovery engine that combines polymer chemistry, biology, and AI, we have achieved lung selectivity of pDNA payload delivery with a single multimonomeric polyelectrolyte nanocarrier from a vast, generative PNP design space. Further polymer chemistry campaigns combined with explanatory polymer microstructure models can potentially expand structure-tropism relationships developed for PNP6 to optimize PNPs for any nucleic acid cargo for cellular delivery (Fig. 4C). Molecular engineering and bioconjugation initiatives to address cell-specific uptake and mucus penetration *in vitro* with cystic fibrosis treatment are in progress. mRNA-based therapeutics are also being incorporated into multicomponent PNPs using this workflow. Further reports will exemplify our vision of combining the ever-evolving precision of polymer synthesis with the expanding repertoire of biologic medicines to offer powerful modalities for non-viral gene delivery and to pioneer new eras of gene therapy.

## Notes

All animal procedures were performed according to the standards of the Association for Assessment and Accreditation of Laboratory Animal Care and to the Guidelines and Use of Laboratory Animals of Biomedical Research Models, Inc. (Worcester, MA, USA). All mouse experiments were approved by the Institutional Animal Care and Use Committee of Biomere Biomedical Research Models, Inc. (Worcester, MA, USA).

## Conflicts of interest

The authors declare the following competing financial interest (s): J. M.T., J. D. F., S. P., T. T.-M., F. O., and S. K. M. have an equity interest in Nanite, Inc. Nanite has filed a patent applications covering aspects of the work described.

## Acknowledgements

We thank Dr Thomas X. Neenan for helpful discussions, Mitch Stern for his support in general automation, Jared Van Reet for his support in general screening, and Dr Shannon R. Petersen for helpful discussions and feedback on graphic design. We thank Joshua McDonald and Cassandra Vongrej for assistance with routine qPCR analysis and describing its procedure in the ESI.† We also gratefully thank Dr Wendy E. Gavin and Seamus O'Brien for assistance running  $^1\text{H}$  NMR spectroscopy experiments.

## References

- 1 C. Sheridan, *Nat. Biotechnol.*, 2023, **41**, 737–739.
- 2 R. Burrows and E. Lambrix, *Vaccine Insights*, 2022, **1**, 191–199.
- 3 F. Alexis, E. Pridgen, L. K. Molnar and O. C. Farokhzad, *Mol. Pharmaceutics*, 2008, **5**, 505–515.
- 4 S.-D. Li and L. Huang, *Mol. Pharmaceutics*, 2008, **5**, 496–504.
- 5 A. Abuchowski, J. R. McCoy, N. C. Palczuk, T. Van Es and F. F. Davis, *J. Biol. Chem.*, 1977, **252**, 3582–3586.
- 6 J. Li and H. Wang, *Nanoscale Horiz.*, 2023, **8**, 1155–1173.
- 7 M. J. Hajipour, R. Safavi-Sohi, S. Sharifi, N. Mahmoud, A. A. Ashkarraan, E. Voke, V. Serpooshan, M. Ramezankhani, A. S. Milani, M. P. Landry and M. Mahmoudi, *Small*, 2023, 2301838.
- 8 M. Torrice, *ACS Cent. Sci.*, 2016, **2**, 434–437.
- 9 F. Wang, J. Lou, X. Gao, L. Zhang, F. Sun, Z. Wang, T. Ji and Z. Qin, *Nano Today*, 2023, **52**, 101943.

10 U. Griesenbach, D. M. Geddes and E. W. F. W. Alton, *Gene Ther.*, 2004, **11**, S43–S50.

11 M. Tranter, Y. Liu, S. He, J. Gulick, X. Ren, J. Robbins, W. K. Jones and T. M. Reineke, *Mol. Ther.*, 2012, **20**, 601–608.

12 R. N. Mitra, M. Zheng and Z. Han, *Wiley Interdiscip. Rev.: Nanomed. Nanobiotechnol.*, 2016, **8**, 160–174.

13 C. A. Maguire, S. H. Ramirez, S. F. Merkel, M. Sena-Esteves and X. O. Breakefield, *Neurotherapeutics*, 2014, **11**, 817–839.

14 S. Uchida and K. Kataoka, *J. Biomed. Mater. Res.*, 2019, **107**, 978–990.

15 R. Kumar, C. F. Santa Chalarca, M. R. Bockman, C. V. Bruggen, C. J. Grimme, R. J. Dalal, M. G. Hanson, J. K. Hexum and T. M. Reineke, *Chem. Rev.*, 2021, **121**, 11527–11652.

16 J. A. Johnson, F. E. Du Prez and E. Elacqua, *Polym. Chem.*, 2022, **13**, 2400–2401.

17 F. S. Bates, M. A. Hillmyer, T. P. Lodge, C. M. Bates, K. T. Delaney and G. H. Fredrickson, *Science*, 2012, **336**, 434–440.

18 J.-L. Reymond, *Acc. Chem. Res.*, 2015, **48**, 722–730.

19 T. B. Martin and D. J. Audus, *ACS Polym. Au*, 2023, **3**, 239–258.

20 E. C. Day, S. S. Chittari, M. P. Bogen and A. S. Knight, *ACS Polym. Au*, 2023, **3**, 406–427.

21 R. Upadhyia, S. Kosuri, M. Tamasi, T. A. Meyer, S. Atta, M. A. Webb and A. J. Gormley, *Adv. Drug Delivery Rev.*, 2021, **171**, 1–28.

22 P. Jain, R. S. Pawar, R. S. Pandey, J. Madan, S. Pawar, P. K. Lakshmi and M. S. Sudheesh, *Biotechnol. Adv.*, 2017, **35**, 889–904.

23 K. Paunovska, C. D. Sago, C. M. Monaco, W. H. Hudson, M. G. Castro, T. G. Rudoltz, S. Kalathoor, D. A. Vanover, P. J. Santangelo, R. Ahmed, A. V. Bryksin and J. E. Dahlman, *Nano Lett.*, 2018, **18**, 2148–2157.

24 J. M. Ting, T. Tamayo-Mendoza, S. R. Petersen, J. Van Reet, U. A. Ahmed, N. J. Snell, J. D. Fisher, M. Stern and F. Oviedo, *Chem. Commun.*, 2023, **59**, 14197–14209.

25 R. Kumar, N. Le, F. Oviedo, M. E. Brown and T. M. Reineke, *JACS Au*, 2022, **2**, 428–442.

26 R. J. Dalal, F. Oviedo, M. C. Leyden and T. M. Reineke, *Chem. Sci.*, 2024, **15**, 7219–7228.

27 O. Boussif, F. Lezoualc'h, M. A. Zanta, M. D. Mergny, D. Scherman, B. Demeneix and J. P. Behr, *Proc. Natl. Acad. Sci. U. S. A.*, 1995, **92**, 7297–7301.

28 D. Sprouse and T. M. Reineke, *Biomacromolecules*, 2014, **15**, 2616–2628.

29 S. Asayama, T. Sekine, H. Kawakami and S. Nagaoka, *Bioconjugate Chem.*, 2007, **18**, 1662–1667.

30 M. H. Allen, M. D. Green, H. K. Getaneh, K. M. Miller and T. E. Long, *Biomacromolecules*, 2011, **12**, 2243–2250.

31 N. J. Treat, D. Smith, C. Teng, J. D. Flores, B. A. Abel, A. W. York, F. Huang and C. L. McCormick, *ACS Macro Lett.*, 2012, **1**, 100–104.

32 A. M. Funhoff, C. F. Van Nostrum, M. C. Lok, M. M. Fretz, D. J. A. Crommelin and W. E. Hennink, *Bioconjugate Chem.*, 2004, **15**, 1212–1220.

33 S. T. Hemp, M. H. Allen, A. E. Smith and T. E. Long, *ACS Macro Lett.*, 2013, **2**, 731–735.

34 S. T. Hemp, M. H. Allen, M. D. Green and T. E. Long, *Biomacromolecules*, 2012, **13**, 231–238.

35 V. Loczenski Rose, F. Mastrotto and G. Mantovani, *Polym. Chem.*, 2017, **8**, 353–360.

36 D. Y. Takigawa and D. A. Tirrell, *Macromolecules*, 1985, **18**, 338–342.

37 S. Y. Wong, N. Sood and D. Putnam, *Mol. Ther.*, 2009, **17**, 480–490.

38 C. Van Bruggen, J. K. Hexum, Z. Tan, R. J. Dalal and T. M. Reineke, *Acc. Chem. Res.*, 2019, **52**, 1347–1358.

39 R. Kumar, N. Le, Z. Tan, M. E. Brown, S. Jiang and T. M. Reineke, *ACS Nano*, 2020, **14**, 17626–17639.

40 Z. Ruan, S. Li, A. Grigoropoulos, H. Amiri, S. L. Hilburg, H. Chen, I. Jayapurna, T. Jiang, Z. Gu, A. Alexander-Katz, C. Bustamante, H. Huang and T. Xu, *Nature*, 2023, **615**, 251–258.

41 M. Reis, F. Gusev, N. G. Taylor, S. H. Chung, M. D. Verber, Y. Z. Lee, O. Isayev and F. A. Leibfarth, *J. Am. Chem. Soc.*, 2021, **143**, 17677–17689.

42 E. Blanco, H. Shen and M. Ferrari, *Nat. Biotechnol.*, 2015, **33**, 941–951.

43 C. L. McCormick and A. B. Lowe, *Acc. Chem. Res.*, 2004, **37**, 312–325.

44 A. W. Fortenberry, P. E. Jankoski, E. K. Stacy, C. L. McCormick, A. E. Smith and T. D. Clemons, *Macromol. Rapid Commun.*, 2022, **43**, 2200414.

45 S. Cosson, M. Danial, J. R. Saint-Amans and J. J. Cooper-White, *Macromol. Rapid Commun.*, 2017, **38**, 1600780.

46 J. M. Ting, H. Wu, A. Herzog-Arbeitman, S. Srivastava and M. V. Tirrell, *ACS Macro Lett.*, 2018, **7**, 726–733.

47 T. A. Tockary, K. Osada, Q. Chen, K. Machitani, A. Dirisala, S. Uchida, T. Nomoto, K. Toh, Y. Matsumoto, K. Itaka, K. Nitta, K. Nagayama and K. Kataoka, *Macromolecules*, 2013, **46**, 6585–6592.

48 A. E. Marras, J. M. Ting, K. C. Stevens and M. V. Tirrell, *J. Phys. Chem. B*, 2021, **125**, 7076–7089.

49 A. E. Marras, J. R. Vieregg, J. M. Ting, J. D. Rubien and M. V. Tirrell, *Polymers*, 2019, **11**, 83.

50 I. Skeist, *J. Am. Chem. Soc.*, 1946, **68**, 1781–1784.

51 J. M. Ting, T. S. Navale, F. S. Bates and T. M. Reineke, *ACS Macro Lett.*, 2013, **2**, 770–774.

52 A. L. Holmberg, M. G. Karavalias and T. H. Epps, *Polym. Chem.*, 2015, **6**, 5728–5739.

53 A. A. A. Smith, A. Hall, V. Wu and T. Xu, *ACS Macro Lett.*, 2019, **8**, 36–40.

54 A. M. Rumyantsev, N. E. Jackson, B. Yu, J. M. Ting, W. Chen, M. V. Tirrell and J. J. de Pablo, *ACS Macro Lett.*, 2019, **8**, 1296–1302.

55 B. Yu, A. M. Rumyantsev, N. E. Jackson, H. Liang, J. M. Ting, S. Meng, M. V. Tirrell and J. J. de Pablo, *Mol. Syst. Des. Eng.*, 2021, **6**, 790–804.

56 C. Fick, Z. Khan and S. Srivastava, *Mater. Adv.*, 2023, **4**, 4665–4678.

57 P. U. Joshi, C. Decker, X. Zeng, A. Sathyavageeswaran, S. L. Perry and C. L. Heldt, *Biomacromolecules*, 2024, **25**, 741–753.

58 M. Yang, Z. A. Digby, Y. Chen and J. B. Schlenoff, *Sci. Adv.*, 2022, **8**, eabm4783.

59 S. Perry, Y. Li, D. Priftis, L. Leon and M. Tirrell, *Polymers*, 2014, **6**, 1756–1772.

60 K. C. Stevens, A. E. Marras, T. R. Campagna, J. M. Ting and M. V. Tirrell, *Macromolecules*, 2023, **56**, 5557–5566.

61 W. Wang, *Int. J. Pharm.*, 2015, **490**, 308–315.

62 J. Huang, L. Knight and J. Laaser, *ChemRxiv*, 2022, pre-print, DOI: [10.26434/chemrxiv-2022-g13t8](https://doi.org/10.26434/chemrxiv-2022-g13t8).

63 K. J. Livak and T. D. Schmittgen, *Methods*, 2001, **25**, 402–408.

64 Y. Cao, Z. He, Q. Chen, X. He, L. Su, W. Yu, M. Zhang, H. Yang, X. Huang and J. Li, *Nano Lett.*, 2022, **22**, 6580–6589.

65 S. A. Dilliard, Q. Cheng and D. J. Siegwart, *Proc. Natl. Acad. Sci. U. S. A.*, 2021, **118**, e2109256118.

66 Y. Huang, J. Wu, S. Li, Z. Liu, Z. Li, B. Zhou and B. Li, *Theranostics*, 2024, **14**, 830–842.

67 M. G. Hanson, C. J. Grimme, N. W. Kreofsky, S. Panda and T. M. Reineke, *Bioconjugate Chem.*, 2023, **34**, 1418–1428.

68 K. Leer, L. S. Reichel, J. Kimmig, F. Richter, S. Hoeppener, J. C. Brendel, S. Zechel, U. S. Schubert and A. Traeger, *Small*, 2024, **20**, 2306116; D. Ulkoski, M. J. Munson, M. E. Jacobson, C. R. Palmer, C. S. Carson, A. Sabirsh, J. T. Wilson and V. R. Krishnamurthy, *ACS Appl. Bio Mater.*, 2021, **4**, 1640–1654.

69 J. Di, P. Huang and X. Chen, *Bioconjugate Chem.*, 2024, **35**, 453–456.

70 T. Montier, P. Delépine, C. Pichon, C. Férec, D. J. Porteous and P. Midoux, *Trends Biotechnol.*, 2004, **22**, 586–592.